Role of refractive index in highly efficient laminated luminescent solar concentrators

23 November 2024

Role of Refractive Index in Highly Efficient Laminated Luminescent Solar Concentrators

Guiju Liu[a,b], Raffaello Mazzaro[c,d], Changchun Sun[b,e], Yuanming Zhang[b,e], Yiqian Wang[a,b,*], Haiguang Zhao[a,b,*], Guangting Han[b,e], Alberto Vomiero[c,f*]

[a] College of Physics, Qingdao University, No. 308 Ningxia Road, Qingdao, 266071, P. R. China

[b] State Key Laboratory of Bio-Fibers and Eco-Textiles, Qingdao University, No. 308 Ningxia Road, Qingdao, 266071, P. R. China

[c] Division of Material Science, Department of Engineering Sciences and Mathematics, Luleå University of Technology, 971 87 Luleå, Sweden

[d] CNR-IMM, Via Piero Gobetti 101, 40129 Bologna, Italy

[e] College of Textiles & Clothing, Qingdao University, No. 308 Ningxia Road, Qingdao, 266071, P. R. China

[f] Department of Molecular Sciences and Nanosystems, Ca' Foscari University of Venice, Via Torino 155, 30172 Mestre Venezia, Italy

Abstract

As a large-area solar radiation collector, luminescent solar concentrators (LSCs) can be used as power generation units in semitransparent solar windows, modernized agricultural greenhouses and building facades. However, the external optical efficiency and long-term stability of the LSCs limit their practical applications due to the sensitivity of the emitters to the light and environmental conditions. Here, we used

the concept of "laminated glass" to prepare LSCs, which consist of two waveguide layers and the quantum dots (QDs)/polymer interlayer, and we tune the refractive index of the different parts of the system to improve the external optical efficiency and stability of the LSCs, simultaneously. The waveguide layer can be glass, quartz, polymethyl methacrylate (PMMA) and other transparent materials. The CdSe/CdS core/shell QDs were used as fluorophores to prepare the interlayer of the LSCs. The external optical efficiency of the laminated LSCs is associated with the refractive index of the three layers: the closer the refractive index, the higher the η_{opt}. The highest external optical efficiency of 3.4% has been achieved for the laminated PMMA/QDs-polymer/PMMA LSCs, which improved ~92% compared to the single-layered CdSe/CdS based LSCs. To the best of our knowledge, this is the highest efficiency for the LSCs based on CdSe/CdS QDs. These results pave the way to realize high efficiency laminated windows as power generation units by suitably tuning the structure of the LSC, and provide the theoretical guidance for the LSCs utilized in building integrated photovoltaics.

1. Introduction

Luminescent solar concentrators (LSCs) have attracted great attention as large-area sunlight collectors for photovoltaics (PVs) because of their light-weight, simple architecture and cost-effective fabrication.[1-5] A typical luminescent solar concentrator (LSC) consists of optical waveguide materials embedded or covered with highly emissive fluorophores (*e.g.* down-shifting or up-converting materials). Upon sun radiating onto the surface of an LSC, the fluorophores re-emit photons and these photons are guided to the device edges by total internal reflection (TIR).[4, 6] Usually, the LSCs coupled with photovoltaic (PV) cells can decrease the usage of expensive PV cells. If the power conversion efficiency (PCE) of the LSCs is high enough (> 6%), the combination of PV cells with LSCs can reduce the cost of solar electricity.[7]

The optical properties of the fluorophores are the most important factors that affect the PCE of the LSCs. They determine the absorption spectral region, the emission wavelength and the reabsorption losses of the LSCs. Colloidal semiconductor quantum dots (QDs) are very attractive fluorophores, which have been recently used as light converter in LSCs due to their tunable absorption and emission properties, high fluorescent quantum yield (QY) and easy preparation.[8-10] Various types of QDs, such as carbon QDs, silicon QDs, core/shell CdSe/CdS QDs, and PbS/CdS QDs are incorporated in polymer slabs for the fabrication of LSCs.[11-15] Compared with the bare QDs, the heterostructured QDs have higher QY, better spectra separation between emission and absorption spectra and improved stability.[13, 16, 17] The application of these QDs has achieved an improvement of the external optical efficiency (η_{opt},

defined as the ratio of the output power from the edges and the input power through the top surface of the LSC) of LSCs. For example, the LSC based on core/shell CdSe/CdS QDs exhibits an enhancement in quantum efficiency (48%) with respect to that of the LSC based on bare CdSe QDs.[13] PbS/CdS QDs based LSCs have the η_{opt} of 6.1% with a geometrical factor (G, defined as the ratio of the top surface area and the lateral area of the LSC) of 10.[14]

Another important factor affecting the performance of the LSCs is their geometric structure. In previous reports about the QDs based LSCs, QDs are embedded in an optical waveguide or coated on the surface of the waveguide, which may limit the efficiency of the device due to the restriction of absorption and emission spectra, and may decrease the long-term stability because of the exposure of some QDs to the environmental atmosphere.[18, 19] Recent studies have improved the performance of LSCs by proposing alternative architectures, for instance, the tandem or sandwich structure, or adding an additional reflection layer (*e.g.* diffuse mirrors).[20-25] In the tandem structure, one layer of LSC based on QDs was stacked on the top of another one and every layer has different emitters with different absorption ranges. The η_{opt} of these LSCs was improved compared to the single-layered structure due to the enhancement of absorption efficiency.[23] Compared with single-layered LSC, the tandem LSCs increase the cost of final electricity due to the increase of the PV material usage and complexity of the fabrication processes. In addition, because the two layers of the LSCs are in direct contact with the surrounding environment, the QDs are easily degraded when the LSCs are exposed to high humidity environment.[18]

Last but not least, some QDs contain toxic elements (*e.g.* Pb and Cd), which may result in health issues if dispersed in the environment. Based on these considerations, we proposed the sandwich structure in our previous work: QDs thin film layer sandwiched between two glass layers to isolate the QDs from surrounding environment (air and water), which improved the η_{opt}, stability and safety, simultaneously.[24] However, obtaining high η_{opt} in large-area LSCs is still a big challenge as (i) the high concentration QDs in the thin film make it difficult to prepare a flat and uniform film, leading to the decrease of η_{opt} because of scattering; (2) the as-prepared sandwich structure is not so mechanical stable as the thin film polymer (in micrometer range) usually cannot cohere the glass very well. Using the concept of "laminated glass", the LSCs can be prepared by replacing the intermediate thin-film layer with thick QDs/polymer layer (up to millimetre) to realize building integrated PVs (BIPVs). Compared to thin film interlayer, the "laminated glass" could offer improved mechanical stability of the LSC and large-scale production using industrial approach; Bergren *et al.* reported the use of this structure for preparation of LSCs based on CuInS$_2$/ZnS QDs[1]; while there is no report for using such structure for CdSe/CdS QDs based LSCs. In addition, in the multilayered structure, there is still less investigation of the relationship between the match of the refractive index (*n*) between layers and the efficiency of the LSCs. Thus, it is of great significance to understand the relationship between *n* and efficiency in laminated LSC for selecting suitable materials to obtain highly efficient LSC.In this work, we prepared laminated LSCs based on CdSe/CdS core/shell QDs by "laminated glass" technology. The

QDs/polymer solution was injected into the gap between two waveguide layers, forming an LSC by *in-situ* polymerization under ultraviolet (UV) light. Through changing the top and bottom layer materials [*e.g.* glass, quartz and polymethyl methacrylate (PMMA)], the relationship between η_{opt} and the match of refractive indexes of different layers in the LSCs has been investigated. The closer the *n* between interlayer and top/bottom layer, the higher the η_{opt} of the LSC. We demonstrate that the combined use of luminophores with large Stokes shift and matrices with matched refractive indexes boosts the overall efficiency of the LSCs. This result could broaden the field of application of LSCs not only to BIPVs, but also to other flexible polymer power roofs.

2. Results and discussion

2.1 The structure of the QDs

CdSe/CdS core/shell QDs were synthesized via a hot injection method followed by a SILAR process at 240 ℃, as described in detail in the experimental section. The structure of the QDs was characterized by TEM, as shown in **Fig. 1a**. From the bright field TEM image, it can be seen that the QDs exhibit a uniform spherical morphology and good dispersion without aggregation. The SAED pattern at the upper right corner of **Fig. 1a** shows that the structure of the QDs is hexagonal wurtzite (WZ) phase. As reported in our previous work, CdSe core QDs exhibit cubic zinc-blende (ZB) structure.[24] Generally, when the shell grows over the core, the structure of the shell materials tends to be consistent with the core. As the shell thickness increases, the strain from the core decreases, and the shell tends to transform into its

thermodynamically stable phase. Ghosh's study has revealed that the thermodynamically stable structure of the CdS under high temperature (240 ℃) is the hexagonal structure, consistent with our results.[26] HRTEM image further identifies the WZ structure of the synthesized QDs, as shown in the inset at the lower right corner of **Fig. 1a**. The lattice spacing of two planes was measured to be ~3.56 Å, and the crossing angle between the two planes is 60°. This means that this QD was viewed along [0001] zone-axis, and the two planes correspond to $(10\bar{1}0)$ and $(01\bar{1}0)$ planes of WZ CdS structure.
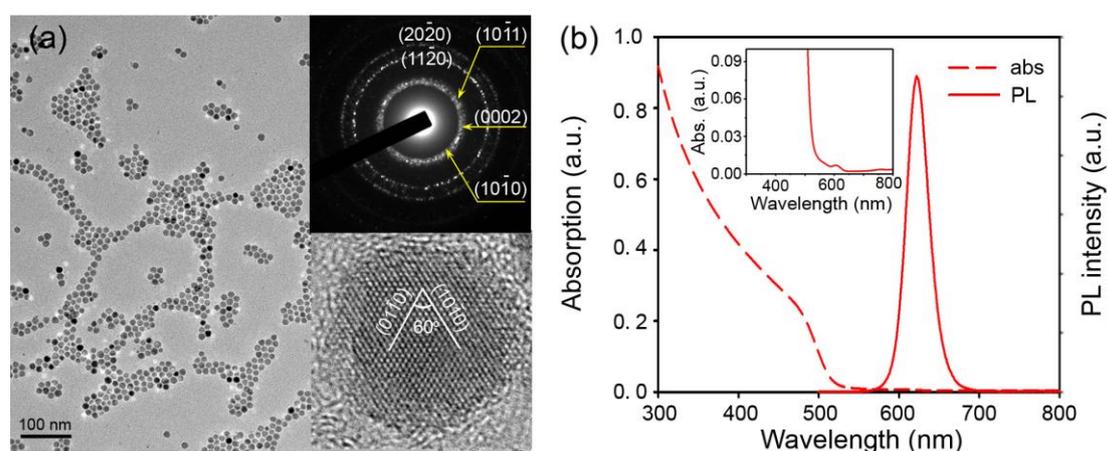
Fig. 1. a) Bright field TEM image of the CdSe/CdS QDs. Insets are the SAED pattern of the QDs and the HRTEM image of an individual QD. b) Absorption and PL spectra of CdSe/CdS QDs. Inset is the locally enlarged absorption spectrum.

2.2 Optical properties of QDs and the LSCs

Fig. 1b shows the absorption and PL spectra of the CdSe/CdS QDs in toluene. The absorption spectrum displays the typical band edge of semiconductor QDs at about 530 nm, indicating that the QDs can absorb the sunlight with a wavelength range from 300 nm to 530 nm, matching well with the solar spectrum from the UV to visible light. It was also characterized by a small bump at about 610 nm (inset in **Fig. 1b**), due to

the weak absorption of CdSe core. The PL spectrum of the QDs exhibits a sharp Gaussian shape with a peak position at 620 nm and a full width at half maximum of 25 nm. The QY of 54.3% was calculated by means of an integrating sphere (λ_{exc}=480 nm) coupled in a PL spectrometer. From the absorption and PL spectra of the QDs, it can be seen that the overlap between the absorption and emission spectra is very small. This means that the reabsorption energy loss can be extremely low when the CdSe/CdS QDs were used as fluorophores in LSCs.
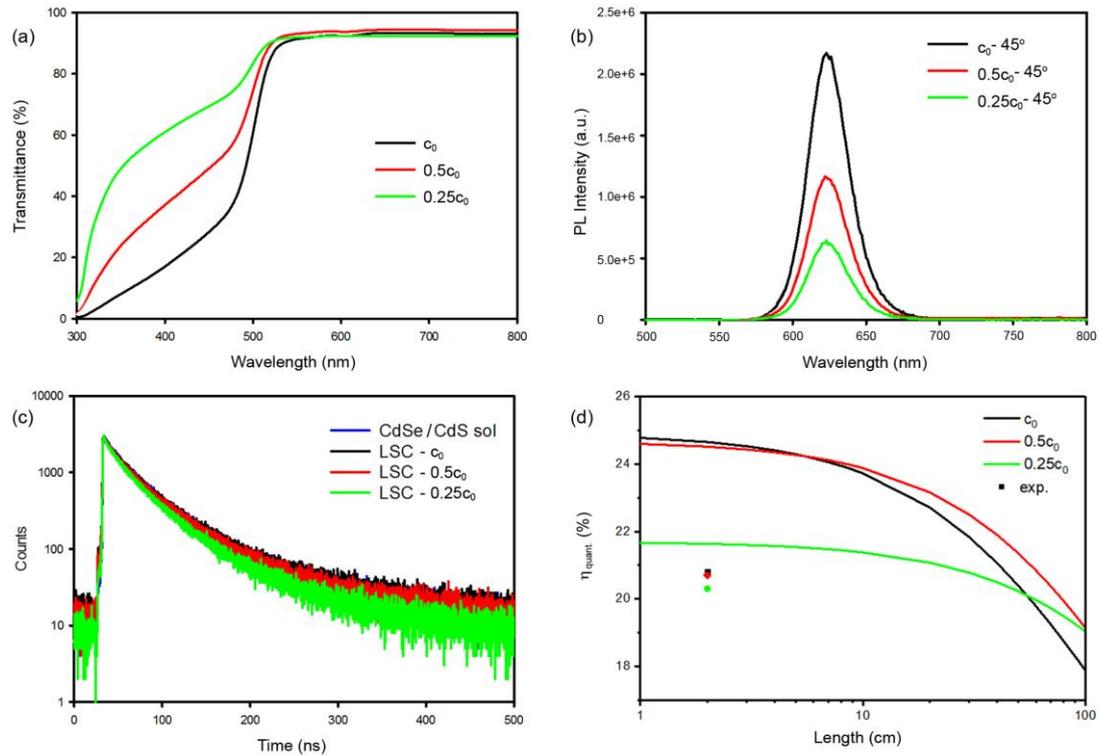
Fig. 2. a) and b) The transmittance and PL intensity spectra of the LSCs with different concentrations of QDs, respectively. c) PL decay curves of the QDs in solution and LSCs. λ_{exc}=480 nm, λ_{em}=620 nm. d) Calculated quantum efficiency (η_{quant}) based on Eq. 4 of the single-layered LSCs with the concentration of QDs increased from $0.25c_0$ to c_0 with the QY=29.1%, 33.1% and 33.4%, respectively.

To obtain high efficiency LSCs, we first regulated the content of QDs in

single-layered LSCs. The single-layered LSCs based on CdSe/CdS QDs were fabricated by incorporating QDs into poly(lauryl methacrylate) (PLMA) polymer. The detailed fabrication process is described in the experimental section. The distribution of QDs in PLMA was characterized by planar scanning electron microscopy (SEM). SEM backscattering diffraction (BSD) image shows that there is no obvious contrast, indicating a uniform device structure (Fig. S2a). The presence of the Cd and S elements was confirmed by two-dimensional energy-dispersive spectroscopy (EDS) mapping of the LSC (Fig. S2b,c). **Fig. 2** shows the optical properties of the LSCs with different concentration of QDs ($0.25c_0$, $0.5c_0$ and c_0). **Fig. 2a** collects the transmittance spectra of the QDs based LSCs. All the three LSCs show very high transmittance (~95%) in the wavelength range of 530-800 nm, proving the good optical quality of the devices. The band edge of the QDs is also recognizable. With increasing QDs content, the light absorption ability of the LSC increases (**Fig. S3a**), thus the transmittance decreases at short wavelength range (<530 nm, determined by the band edge absorption). Partial absorption of the sunlight modifies the color coordinate of light transmitted through the LSCs. To quantify the color of the light transmitted by the LSC, we analyzed the color rendering index (CRI) following the International Commission on Color (CIE) 1931 parameters, as shown in **Fig. S3b**. It clearly shows different color coordinates with different contents of QDs. This means that we can control the concentration of the QDs to regulate the color of the LSC, to meet the visual comfort of individuals residing in the building and the specific requirements for indoor illumination.

Fig. 2b and **Fig. S4** show the PL spectra of the LSCs with different QDs concentration. The spectra are measured with two configurations (45° and 90°) as shown in the schematic diagram in **Fig. S4a**. No shift of the PL spectra can be observed with respect to that in toluene (**Fig. 1b**). For all the samples, only the emission intensity changes, while the band shape remains the same, indicating that no re-absorption processes occur. The variation of PL intensity is associated with the content of QDs in the LSC. With decreasing QDs concentration, the PL intensity reduces due to the decreased LSC absorption (**Fig. S3a**). The QY of the QDs exhibits no significant changes especially for the LSCs with QDs concentration of c_0 and $0.5c_0$ (**Table 1**), while a significant drop is observed with respect to that in solution-phase. The UV light could accelerate the surface reaction of quantum dots, leading to the increase number of surface defects, which lead to the drop of QY. The photo-stability of the LSC can be characterized by the PL intensity as a function of UV illumination time. As shown in **Fig. S5**, the integrated PL intensity decreases quickly after the first 10 min upon UV light illumination and then maintains a stable value. After 2 h of continuous UV light illumination, the PL intensity of the single layer LSC maintained 82% of its initial value, indicating a good photo-stability of the LSC. The PL decay curves of the QDs in LSCs and solution are shown in **Fig. 2c**, which can be fitted by three exponential decay curves. The lifetimes for each component are summarized in Table 1, as well as the pre-exponential factor and the average lifetime. The average lifetime ($\bar{\tau}$) was calculated as follows: [27]

$$\bar{\tau} = \frac{A_1\tau_1^2 + A_2\tau_2^2 + A_3\tau_3^2}{A_1\tau_1 + A_2\tau_2 + A_3\tau_3} \tag{1}$$

in which A_1, A_2 and A_3 are the fitting coefficients, and τ_1, τ_2 and τ_3 are the characteristic lifetimes of the three PL decay components, respectively. Compared with the decrease of QY, the average lifetime of the QDs in LSC shows a negligible decrease with respect to the one in solution.

Table 1 QY and lifetime of the QDs in LSCs and solution.

Sample	QY (%)	A_1	τ_1 (ns)	A_2	τ_2 (ns)	A_3	τ_3 (ns)	$\bar{\tau}$(ns)
solution	54.3	449	8.2	1968	30.0	619	69.9	46.5
c_0-LSC	33.4	456	7.1	1698	26.9	783	65.7	46.2
0.5c_0-LSC	33.1	460	7.7	1699	27.7	671	67.0	45.4
0.25c_0-LSC	29.1	850	10.1	1784	33.3	225	93.4	45.2

2.3 Optical efficiency of LSCs

The performance of the LSCs was then measured using an integrating sphere with the scheme illustrated in **Fig. S1**. By masking all the lateral edges of the LSC, it is possible to calculate the single frequency η_{quant} (see details in the experimental section). The experimental and theoretical results of η_{quant} for the LSCs are shown in **Fig. 2d** and **Table S1**. It can be seen that the η_{quant} of the LSC with the QDs concentration of c_0 is very close to that with QDs concentration of 0.5c_0. When the content of QDs decreases to 0.25c_0, the η_{quant} shows a slight decrease due to the lower QDs concentration. This trend is consistent with the theoretical result obtained using equation (5), as shown in **Fig. 2d**. From the theoretical results, we can see that the

η_{quant} is close for the small-area LSC with the QDs concentration of c_0 and $0.5c_0$, but it drops faster for the LSC with higher concentration of QDs in large-scale device, due to the reabsorption energy loss. The η_{opt} is associated with the η_{quant} and η_{Abs} [equation (3)]. In a certain range, with increasing QDs contents, the η_{Abs} increases, and the η_{opt} also improves. Thus, we selected the QDs/PLMA mixture with a QD concentration of c_0 as the interlayer to prepare the laminated LSC.
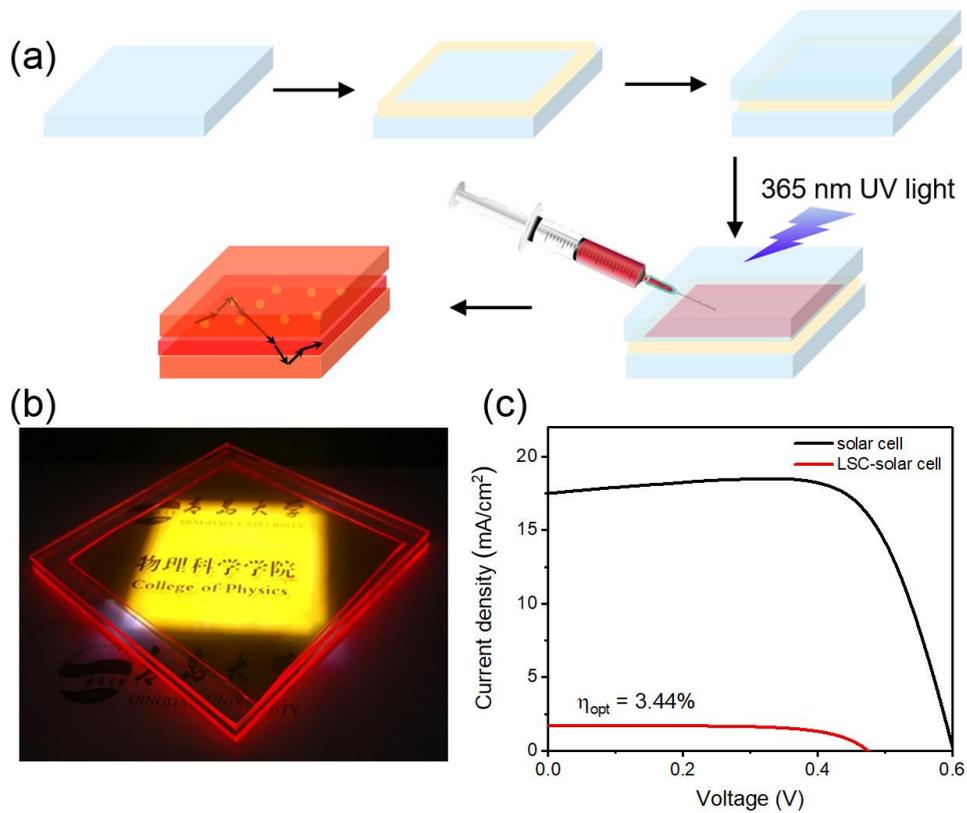

Fig. 3. a) Schematic diagram of fabrication process for a laminated LSC. b) Photograph of the prepared LSC ($8\times8\times0.7$ cm^3) under one sun illumination. c) *J-V* curve of the LSC upon natural sunlight illumination (~53 mW/cm^2).

Fig. 3a illustrates the fabrication process of the laminated LSC. Firstly, a silicon rubber spacer with a square empty space was placed on the waveguide (glass, quartz or PMMA), and then it was covered with another identical waveguide, forming an

integrated mold. Then the QDs/PLMA solution was injected into the mold. Finally, the laminated LSC was prepared under a 365 nm UV light radiation for 1 h. An example of the laminated LSC is shown in **Fig. 3b**, which is the LSC (8×8 cm^2) with a structure of PMMA/QDs-PLMA/PMMA under one sun illumination (100 mW/cm^2). Red light can be clearly observed at the edges in all the three layers, indicating that the emitted light can be transmitted through the whole device. Similar phenomena can be found for other types of laminated LSCs using the glass (or quartz) as top and bottom layers. **Fig. 3c** collects the *J-V* curve of this LSC under natural sunlight illumination (~53 mW/cm^2). During the measurement, the spacer of the LSC was removed. The Si solar cell was coupled with the lateral side of the LSC where the edge of the interlayer coincided with the edge of top/bottom layer (*i.e.* the lateral side without spacer during preparation). The η_{opt} of this LSC is measured to be ~3.44%, higher than the similar CdSe/CdS QDs based LSCs in previous reports.[24,28] **Fig. S6** shows the *J-V* curve of a single-layered LSC. From this curve, the η_{opt} of the single-layered LSC can be calculated as 1.79%, which means that compared to the single-layered LSC, the η_{opt} of laminated LSC exhibits a 92% enhancement. This improvement of the efficiency for LSCs is mainly attributed to the architecture of the devices. In the traditional single-layered LSCs, the emitted light intensity from QDs may be decreased during its propagation in the LSC by TIR due to the reabsorption loss of the QDs, as shown in **Fig. S7a**. However, in the laminated LSCs, some of the emitted light can be propagated in the top/bottom layer waveguide, where there are no QDs or other defects and thus no reabsorption loss occurs when light propagates in

these layers. In addition, as the thickness of the laminated LSC increases, the G factor of the device decreases. Therefore, the η_{opt} of the laminated LSCs is enhanced compared to that for single-layered LSCs.

To quantitatively analyze the portion of the light propagated in the interlayer and top/bottom layer, we measured the J-V curves of the LSC by masking some edges of the LSC, as shown in **Fig. 4**. When measuring the J-V curves at the interlayer, the edges of the top and bottom layers were masked by black tapes. Similarly, when measuring the J-V curves at the top or bottom layer, the edges of the other two layers were masked by black tape. Considering the n variation of the interlayer and top/bottom layer, two configurations are possible for the LSC: $n_{inter}<n_{top}$ (**Fig. 4a**) and $n_{inter}>n_{top}$ (**Fig. 4b**). When $n_{inter}<n_{top}$, the current of the top (or bottom) layer is approximately twice that of the interlayer (**Fig. 4a**), which is consistent with the thickness ratio between top (or bottom) layer and interlayer, indicating that the current density of interlayer is approximately equal to that of top (or bottom) layer. The uniform current density of the three layers is attributed to the same probability of the light distribution at the edges (**Fig. S7b**). However, when $n_{inter}>n_{top}$, the current of the top (or bottom) layer is about 2.3 times that of the interlayer (**Fig. 4b**), which is less than 3 times that of the interlayer [the thickness ratio between the top (or bottom) layer and interlayer is 3:1]. Therefore, the current density of interlayer is higher than that of the top (or bottom) layer, as a result of the more efficient light trapping in the interlayer (**Fig. S7c**). In this case, the current of the interlayer originates from two parts of light: the total reflected light only in the interlayer (red arrows in **Fig.S7c**),

and the part distributed in the interlayer of the total reflected light propagation in the whole LSC (green arrows in **Fig. S7c**), as a result of higher light density emitted at the interlayer, which leads to a higher current density of this region. However, more light propagation in the interlayer may suffer from more reabsorption loss which leads to the quicker decrease of the η_{opt} for the large-area LSCs compared to that in the case of $n_{inter} < n_{top}$.
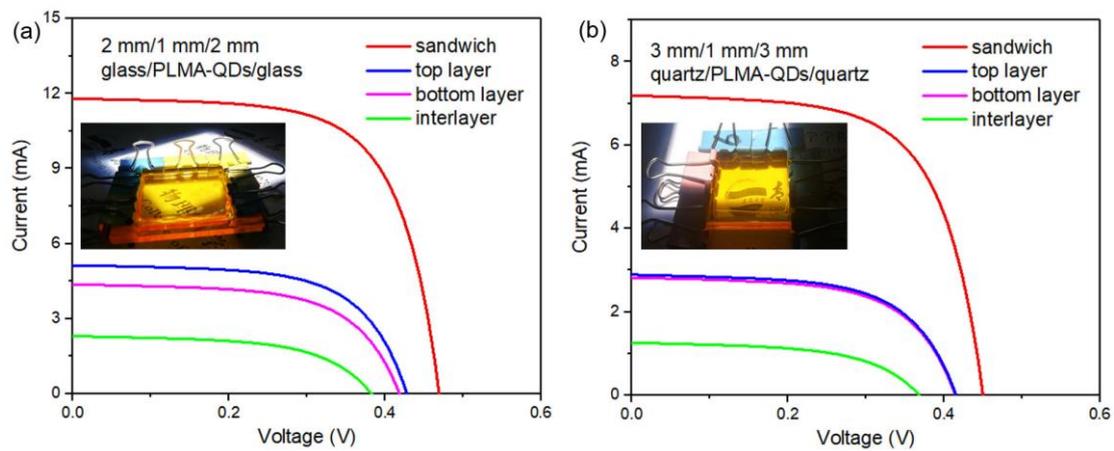

Fig. 4. *J-V* curves of the laminated LSCs (red) with the structure of glass/QDs layer/glass a) and quartz/QDs layer/quartz b), and the same type of PV cells attached to the top (blue), bottom (pink) layer or interlayer (green) under one sun illumination (100 mW/cm^2). The dimensions of the two LSCs are $3.5 \times 3.5 \times 0.5$ cm^3 and $3.5 \times 3.5 \times 0.7$ cm^3, respectively.

To clarify the difference of the two cases, and to predict the most appropriate n_{top} for laminated LSCs when the n_{inter} is fixed, we calculated the η_{opt} of the laminated LSC with different n_{top}, as shown in **Fig. 5**. **Fig. 5a** shows the absorption spectrum of the LSC and the solar spectrum according to the AM1.5G standard. The shadow region represents the fraction of sunlight absorbed by the LSC, which is ~14.1% of the total solar spectral energy. For all the LSCs (single-layered and laminated

structure with different refractive indexes), the parameters related to the QDs layer remain constant, including QDs concentration, thickness and lateral area, as well as the absorption properties of the LSCs. Based on the equations (3)-(7), we calculated the η_{opt} of the laminated LSCs with different n_{top}. The refractive index of QDs/PLMA layer (n_{inter}) was measured to be ~1.50. The refractive indexes of glass, PMMA and quartz (n_{top}) were measured to be 1.51, 1.49 and 1.45, respectively (**Table S2**). Since the n_{top} for the three waveguides at 589 nm is very similar to that at 620 nm (PL peak position), the measured n_{top} was used to calculate the η_{opt} of the laminated LSCs. **Fig. 5b** shows the experimental and theoretical results of the laminated and single-layered LSCs with different n_{top}. In the calculation, the QY of the QDs was set as 33%, which is consistent with the experimental results. The η_{opt} of the laminated LSC is higher than that of single-layered LSC, which is attributed to the decrease of G factor and the reduction of reabsorption loss (**Fig. S7**). For the laminated LSCs, the η_{opt} shows a dependence on n_{top}, which is also observed when simulating the behavior with a QY of 100% (**Fig. 5c**). When the lateral size is small (<10×10 cm^2), the η_{opt} has no obvious change with different n_{top}. On the contrary, for the large-area laminated LSCs (>10×10 cm^2), the η_{opt} begins to show significant differences when the area increases. Compared to the case of $n_{inter}<n_{top}$, the downward trend of the η_{opt} for the case of $n_{inter}>n_{top}$ is more pronounced and the η_{opt} is lower for large-area LSCs indicating that the n can affect the performance of the LSCs. **Fig. 5d** shows the change of η_{opt} with the increase of n_{top} (n_{inter} is maintained 1.50, QY=100%). It clearly shows the dependence of the η_{opt} on the n_{top} for the laminated LSCs. With increasing n_{top}, the η_{opt}

increases quickly first and then decreases slowly. Generally, for the LSCs with same dimension, the η_{opt} in the case of $n_{inter}<n_{top}$ is higher than that in the case of $n_{inter}>n_{top}$. The closer the n between interlayer and top/bottom layer is, the higher the η_{opt} is. When the QY decreases to 50%, the η_{opt} keeps the same trend as the change of refractive index (**Fig. S8**).
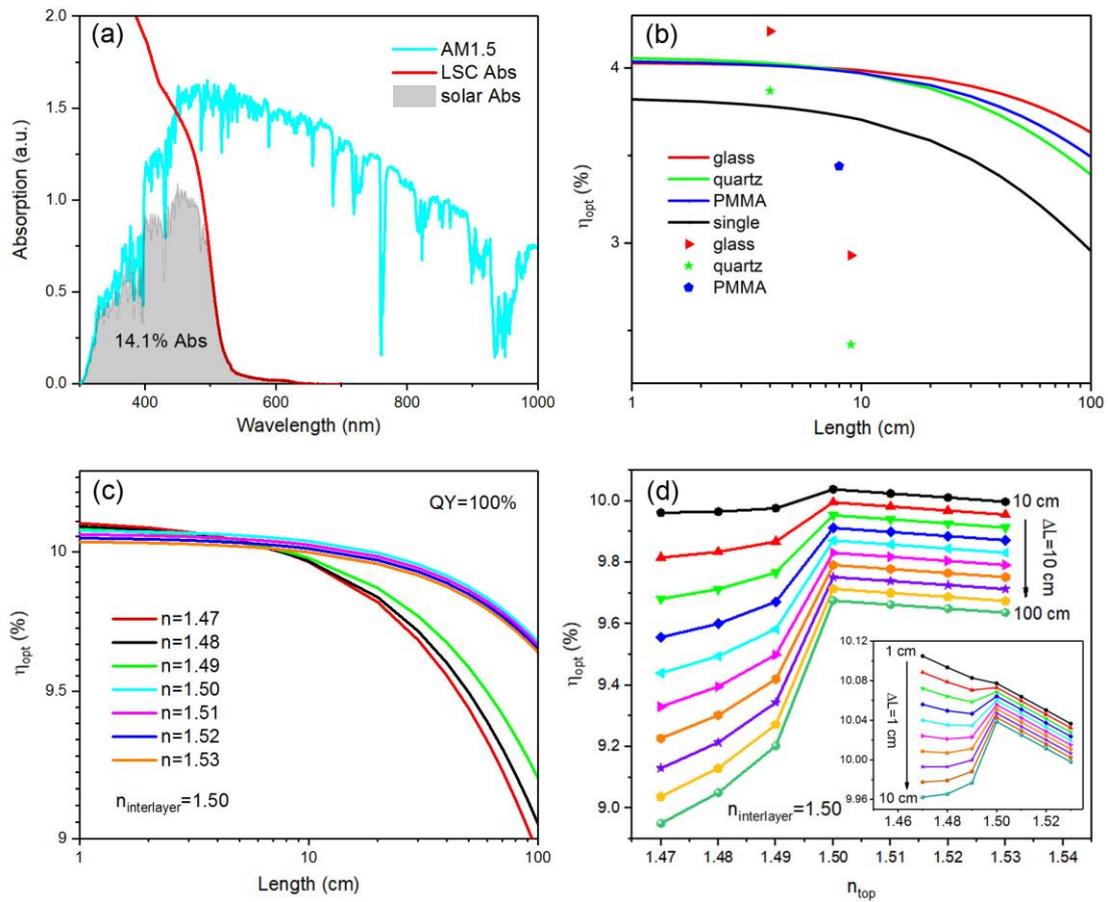

Fig. 5. a) Absorption spectrum of CdSe/CdS QDs used in LSC along with the AM 1.5 G solar spectrum. b) η_{opt} of the laminated and single-layered LSCs under one sun illumination, with the experimental QY (33%). c) η_{opt} of the laminated LSCs with ideal QY = 100%. d) η_{opt} of the laminated LSCs with different n_{top}, QY = 100%.

To clarify the different behaviors of the LSCs with different refractive indexes, we analyzed the propagation of re-emitted light in LSCs, as shown in **Fig. S7**. When $n_{inter}<n_{top}$, the emitted light from interlayer can be refracted into the top and bottom

layers. Some light will escape when the angle is lower than the escape cone, and the rest will be reflected back to the interlayer and propagates in the whole structure following the TIR, as shown in **Fig. S7b**. In this case, the light propagating in the top and bottom layer will not induce reabsorption loss due to the lack of QDs or other defects, which can improve the η_{opt} of the large-area LSC, although the light propagation in the interlayer still causes reabsorption loss by the QDs. When $n_{inter}>n_{top}$, some of the emitted light from interlayer can be refracted into the top and bottom layers and others will be trapped in the interlayer due to the TIR (**Fig. S7c**). The part of the light propagating in the whole LSC has similar characteristics of reabsorption loss to that in the case of $n_{inter}<n_{top}$. The part of light trapped in the interlayer, instead, has the same characteristics as that in single-layered LSC, suffering from reabsorption loss. Thus, the total reabsorption loss in the case of $n_{inter}>n_{top}$ is larger than that in the case of $n_{inter}<n_{top}$, leading to a lower η_{opt} for large-area LSCs.

Besides the optical efficiency, the long-term stability of the LSC is another critical issue for the practical usage of the LSC. Thus, we investigated the performance changes of the laminated and single-layered LSCs after one year of indoor storage under natural conditions [atmosphere and humidity (20%-90% for Qingdao, China this year)]. As shown in Fig. S9, the η_{opt} of the laminated LSC (PMMA/PLMA-QDs/PMMA structure) was measured to be ~3.13%, maintaining ~91% of its initial value (3.44%). While for the single-layered LSC, the η_{opt} only remains ~86% of its initial value, which is lower than that in laminated structure. The better stability of the laminated LSC is attributed to its special structure, that is, the

QDs layer is sandwiched between two stable waveguide layers to avoid the side effect of atmosphere and humidity on the QDs. In addition, we also measured the change of PL intensity under continuous UV illumination (4 W, 0.2 cm from LSC to lamp). As shown in Fig. S5, both the single-layered and laminated LSCs have similar photo-stability characteristics: after a first 10-15% drop during the initial 10-20 mins, the PL intensity stabilizes and no further photo-degradation is observed. Again, the laminated LSC shows a better photo-stability (maintains 86% vs. 81%), due to the better protection from the glass encapsulation.

Overall, the laminated LSCs exhibit an improved η_{opt} over the single-layered LSCs and the laminated LSCs with $n_{inter}<n_{top}$ show higher η_{opt} compared to that in the case of $n_{inter}>n_{top}$. The main reasons are as follows: 1) compared to single-layered LSCs, reabsorption loss and G factor in the laminated LSCs were reduced; 2) in laminated LSCs, compared to the case of $n_{inter}>n_{top}$, when $n_{inter}<n_{top}$, the LSCs suffer less reabsorption loss due to lower re-emitted light propagation in the QDs layer. In addition, similar to our previous report about the film based sandwich structure LSCs[23], the laminated LSCs have better stability compared with single-layered LSCs, attributed to the architecture of the LSCs, which confines the QDs in the interlayer region, avoiding the direct contact between QDs and ambient environments. This study indicates that the sandwich structure can be used in thicker QDs interlayer based LSCs. Through tuning the n of interlayer and top/bottom layer, the controllable preparation of high η_{opt} LSCs in various application fields can be achieved.

3. Conclusion and perspectives

In summary, CdSe/CdS core/shell QDs were used to prepare laminated LSCs, in which QDs/PLMA layer was laminated between two identical waveguides (glass, quartz or PMMA). Compared to the thin-film geometry, the laminated structure offers the benefit of optimization of the best matches between the QDs interlayer and the out-layer in order to obtain highest efficiency of the LSCs. The laminated LSCs exhibit better η_{opt} than single-layered LSCs, due to the reduction of reabsorption loss and the decrease of G factor. In laminated LSCs, as the top surface area increases, the reduction trend of η_{opt} strongly depends on the match of n between adjacent layers. For large-area LSCs, the η_{opt} in the case of $n_{inter}<n_{top}$ is higher than that in the case of $n_{inter}>n_{top}$, mainly attributed to the decrease of reabsorption loss in QDs interlayer. The closer the n of the three layers, the higher η_{opt} of the LSC. This finding proposes an n-engineered LSC, highlighting the importance of the choice of proper materials in a multilayered structure to improve the overall device efficiency. The experimental validation of the concept demonstrates a promising pathway to achieve high-efficiency LSCs in different application places, such as BIPVs, plastic greenhouses and other places, where external sunlight illumination is required. This concept could be applied to other fluorophores (*e.g.* perovskite nanocrystals; carbon dots; upconversion nanocrystals) which is sensitive to the moisture and environmental conditions.

4. Experimental Section

4.1 Materials

Selenium pellet (Se, ≥99.999%), lauryl methacrylate monomer (LMA), ethylene

glycol dimethacrylate (EGDM), diphenyl(2,4,6-trimethylbenzoyl)phosphine oxide (TPO), hexane, toluene, methanol, and ethanol were purchased from Sinopharm Chemical Reagent Co. Ltd.. Sulphur (S, 100%), oleylamine (OLA), oleic acid (OA), and octadecene (ODE), Cadmium oxide (CdO, 99%), trioctyl phosphine oxide (TOPO) and trioctyl phosphine (TOP, 97%) were purchased from Sigma-Aldrich. All chemicals were used as purchased.

4.2 Synthesis of CdSe/CdS core/shell QDs

The CdSe QDs were first synthesized by hot injection approach and then CdS shell was covered over the CdSe core by a successive ionic layer adsorption and reaction (SILAR) method, as reported in previous literature [24]. In detail, 1 mL $Cd(OA)_2$ (0.38 mmol) and 1 g TOPO in 8 mL ODE were purged by N_2 at 110 ℃ for 30 min. Then the mixture of Se (320 mg), TOP (4 mL), OLA (3 mL) and ODE (1 mL) at room temperature was quickly injected into the $Cd(OA)_2$ precursor solution when the solution was raised to 300 ℃. After 5 min reaction, the solution was quenched with ice water. The CdSe core QDs were obtained after centrifugation and purification by ethanol. Subsequently, the CdS shell was coated over the core. Firstly, the mixture of OLA (5 mL), ODE (5 mL) and CdSe QDs (~ 2×10^{-7} mol in hexane) was degassed at 110 °C for 30 min. Then the temperature was raised to 240 ℃ in N_2 atmosphere. Secondly, the $Cd(OA)_2$ dispersed in ODE (0.25 mL, 0.2 M) was added dropwise and reacted for 1 h, and then 0.2 M S in ODE with same volume was added dropwise and reacted for 10 min at 240 °C. Thirdly, repeat step two with several times with different injection volumes. The addition volumes of $S/Cd(OA)_2$ for shell addition cycles 1-15

were as follows: 0.25, 0.36, 0.49, 0.63, 0.80, 0.98, 1.18, 1.41, 1.66, 1.92, 2.20, 2.51, 2.83, 3.17 and 3.53 mL, respectively. Lastly, the QDs solution was cooled down to room temperature using ice water. The QDs were dispersed in toluene for further characterization after purification by centrifugation.

4.3 Preparation of laminated LSCs

LMA and EGDM were mixed with a mass ratio of 85:15. Then the mixture solution was mixed with a UV initiator TPO (0.35 wt.%). Subsequently, the solution was mixed homogeneously with solvent free CdSe/CdS QDs. For single-layered LSCs, the mixture was injected into a mold, which is made up of two pieces of glass separated by a silicon rubber spacer. For laminated LSCs, the mixture was injected into an empty slot consisting of two identical waveguide plates. Then, the mixture was kept under UV light illumination for 1 h. In this work, the waveguide plates are glass, quartz and PMMA, respectively. The transmittances of these waveguides are shown in **Fig. S10** indicating that the UV light (~350 nm) used for polymerization can pass through them. The dimensions of the LSCs are $2\times2\times0.1$ cm^3 and $8\times8\times0.1$ cm^3 for single-layered LSCs; $3.5\times3.5\times0.5$ cm^3, $3.5\times3.5\times0.7$ cm^3, $8\times8\times0.5$ cm^3 and $8\times8\times0.7$ cm^3 for laminated LSCs with the 0.1 cm-thick interlayer, respectively.

4.4 Characterizations

Transmission electron microscopy (TEM), high-resolution TEM (HRTEM) and selected-area electron diffraction (SAED) measurements were carried out using a JEOL JEM 2100Plus TEM operating at 200 kV. SEM BSD image and EDS mapping were characterized by a field emission SEM (Sigma 500 SEM) coupled with EDS

equipment (INCAx-Sight 6427 EDS). Absorption spectra were recorded using a double beam Agilent Cary-5000 UV-Vis-NIR spectrophotometer. Photoluminescence (PL) characterization of the QDs was performed on an Edinburgh FLS980 single photon counting fluorometer. QY was measured with De Mello method by employing a PTFE coated integrating sphere.[29] Refractive index measurements were performed by Abbe refractometer (WAY-2S) with a sodium lamp (Na$_D$ line λ=589 nm).

The η_{opt} of the LSCs was measured under natural sunlight illumination or solar simulator illumination. The solar simulator at AM 1.5G was calibrated through a Si calibrated solar cell to be 100 mW/cm^2. The intensity of the natural sunlight at Qingdao, China was measured using a Si calibrated solar cell (IXYS KXOB22). During measurement, a Si solar cell, preliminarily tested upon direct illumination at AM 1.5G, was positioned at one side of the LSC edges to absorb the concentrated light (the active area for the edge of the LSC is that covered by the solar cell). Due to the geometry of the Si solar cell, the distance between the LSC and the solar cell is ~1 mm. The current-voltage (*J-V*) characteristics of the LSC were measured by a Keysight 2900A Source Meter under simulated sunlight using a solar simulator at AM 1.5G. The η_{opt} of the LSCs can be calculated as the following equation: [30]

$$\eta_{opt} = \frac{J_{LSC}}{J_{SC} \times G} \tag{2}$$

where J_{LSC} and J_{SC} are the short circuit current density from the solar cell attached to the edge of the LSC and the same solar cell under direct sunlight illumination, respectively. *G* is the geometric factor.

The quantum optical efficiency (η_{quant}) was calculated by employing the method

proposed by Coropceanu *et al.* [13]. Briefly, the previously measured QY of the device is compared with the QY of the same device obtained by masking the edges of the LSC with black tape (QY$_m$), as shown in **Fig. S1**. The η_{quant} can be calculated as the difference between the QY and QY$_m$, *i.e.* $\eta_{quant} = QY - QY_m$.

Theoretical calculation of the η_{opt} for laminated LSC: The η_{opt} of the LSC can be expressed as the following equation: [19]

$$\eta_{opt} = \eta_{Abs} \times \eta_{quant} \tag{3}$$

where η_{Abs} is the absorption efficiency of the LSC and η_{quant} is the internal quantum efficiency of the LSC. The η_{Abs} of the LSC can be calculated as: [19]

$$\eta_{Abs} = (1 - R) \frac{\int_0^\infty I_{in}(\lambda)(1 - e^{-\alpha(\lambda)d})d\lambda}{\int_0^\infty I_{in}(\lambda)d\lambda} \tag{4}$$

where $I_{in}(\lambda)$ is the solar irradiation, $\alpha(\lambda)$ is the absorption coefficient $[\alpha(\lambda) = \ln(10)\frac{A(\lambda)}{d}$, in which $A(\lambda)$ is the absorption of the LSC, and d is the thickness of the interlayer in LSC]. R is the reflection coefficient, which is associated with the n of the LSC top/bottom slab (n_{top}). R can be calculated as:

$$R = (n_{top} - 1)^2 / (n_{top} + 1)^2.$$

Generally, the η_{quant} of the LSC can be expressed as: [19]

$$\eta_{quant} = \frac{\int_0^\infty \frac{\eta_{QY}\eta_{trap}}{1 + \beta\alpha(\lambda)L(1 - \eta_{QY}\eta_{trap})} I_{PL}(\lambda)d\lambda}{\int_0^\infty I_{PL}(\lambda)d\lambda} \tag{5}$$

where η_{QY} is the QY of the QDs in LSCs with a lateral size of 1×1 cm^2, I_{PL} is the PL emission spectrum of the LSC, the β factor is a numerical value fixed to 1.4 as reported by Klimov [19], L is the length of the LSC, and η_{trap} is the efficiency of light

trapping into the LSC, which is associated with the n of the waveguide.

For the laminated LSC, when the n of the QDs interlayer (n_{inter}) is lower than that of top/bottom layer (n_{top}), *i.e.* $n_{inter}<n_{top}$, η_{trap} can be expressed as $\eta_{trap} = \sqrt{1-(\frac{1}{n_{inter}})^2}$. The η_{quant} can be calculated as:

$$\eta_{quant} = \frac{\int_0^\infty \frac{\eta_{QY}\eta_{trap}}{1+\beta\alpha(\lambda)\frac{d}{D}L(1-\eta_{QY}\eta_{trap})}I_{PL}(\lambda)d\lambda}{\int_0^\infty I_{PL}(\lambda)d\lambda} \tag{6}$$

where D is the thickness of the whole LSC.

While when $n_{inter}>n_{top}$, the light trapped in the LSC can be divided into two parts: the total reflection of light in the interlayer (η_{trap2}) and the total reflection of light in the entire LSC (η_{trap1}). In this case, the η_{quant} can be calculated as:

$$\eta_{quant} = \frac{\int_0^\infty \frac{\eta_{QY}\eta_{trap1}}{1+\beta\alpha(\lambda)\frac{d}{D}L(1-\eta_{QY}\eta_{trap1})}I_{PL}(\lambda)d\lambda}{\int_0^\infty I_{PL}(\lambda)d\lambda} + \frac{\int_0^\infty \frac{\eta_{QY}\eta_{trap2}}{1+\beta\alpha(\lambda)L(1-\eta_{QY}\eta_{trap2})}I_{PL}(\lambda)d\lambda}{\int_0^\infty I_{PL}(\lambda)d\lambda} \tag{7}$$

in which $\eta_{trap2} = \sqrt{1-(\frac{n_{top}}{n_{inter}})^2}$ and $\eta_{trap1} = \sqrt{1-(\frac{1}{n_{inter}})^2} - \sqrt{1-(\frac{n_{top}}{n_{inter}})^2}$.

References

[1] M. R. Bergren, N. S. Makarov, K. Ramasamy, A. Jackson, R. Guglielmetti, H. McDaniel, High-performance $CuInS_2$ quantum dot laminated glass luminescent solar concentrators for windows, ACS Energy Lett. 3 (2018) 520-525.

[2] L. J. Brennan, F. Purcell-Milton, B. McKenna, T. M. Watson, Y. K. Gun'ko, R.C. Evans, Large area quantum dot luminescent solar concentrators for use with dye-sensitised solar cells, J. Mater. Chem. A 6 (2018) 2671-2680.

[3] D. Cambie, F. Zhao, V. Hessel, M.G. Debije, T. Noel, A leaf-inspired luminescent solar concentrator for energy-efficient continuous-flow photochemistry, Angew. Chem. Int. Edit. 56 (2017) 1050-1054.

[4] M. J. Currie, J. K. Mapel, T. D. Heidel, S. Goffri, M. A. Baldo, High-efficiency organic solar concentrators for photovoltaics, Science 321 (2008) 226-228.

[5] C. Corrado, S.W. Leow, M. Osborn, E. Chan, B. Balaban, S. A. Carter, Optimization of gain and energy conversion efficiency using front-facing photovoltaic cell luminescent solar concentratordesign, Sol. Energ. Mat. Sol. C. 111 (2013) 74-81.

[6] F. Meinardi, Q. A. Akkerman, F. Bruni, S. Park, M. Mauri, Z. Dang, L. Manna, S. Brovelli, Doped halide perovskite nanocrystals for reabsorption-free luminescent solar concentrators, ACS Energy Lett. 2 (2017) 2368-2377.

[7] F. Meinardi, H. McDaniel, F. Carulli, A. Colombo, K. A. Velizhanin, N. S. Makarov, R. Simonutti, V. I. Klimov, S. Brovelli, Highly efficient large-area colourless luminescent solar concentrators using heavy-metal-free colloidal quantum dots, Nat. Nanotechnol. 10 (2015) 878-885.

[8] C. S. Erickson, L. R. Bradshaw, S. McDowall, J. D. Gilbertson, D. R. Gamelin, D.

L. Patrick, Zero-reabsorption doped-nanocrystal luminescent solar concentrators, ACS Nano 8 (2014) 3461-3467.

[9] W. Chen, J. Li, P. Liu, H. Liu, J. Xia, S. Li, D. Wang, D. Wu, W. Lu, X. W. Sun, K. Wang, Heavy metal free nanocrystals with near infrared emission applying in luminescent solar concentrator, Solar RRL 1 (2017) 1700041.

[10] R. Mazzaro, A. Vomiero, The renaissance of luminescent solar concentrators: The role of inorganic nanomaterials, Adv. Energy Mater. 8 (2018) 1801903.

[11] Z. Wang, X. Zhao, Z. Guo, P. Miao, X. Gong, Carbon dots based nanocomposite thin film for highly efficient luminescent solar concentrators, Org. Electron. 62 (2018) 284-289.

[12] F. Meinardi, S. Ehrenberg, L. Dhamo, F. Carulli, M. Mauri, F. Bruni, R. Simonutti, U. Kortshagen, S. Brovelli, Highly efficient luminescent solar concentrators based on earth-abundant indirect-bandgap silicon quantum dots, Nat. Photonics 11 (2017) 177-185.

[13] I. Coropceanu, M. G. Bawendi, Core/shell quantum dot based luminescent solar concentrators with reduced reabsorption and enhanced efficiency, Nano Letter 14 (2014) 4097-4101.

[14] Y. Zhou, D. Benetti, Z. Fan, H. Zhao, D. Ma, A. O. Govorov, A. Vomiero, F. Rosei, Near infrared, highly efficient luminescent solar concentrators, Adv. Energy Mater. 6 (2016) 1501913.

[15] R. Mazzaro, A. Gradone, S. Angeloni, G. Morselli,P. G. Cozzi, F. Romano, A. Vomiero, P. Ceroni, Hybrid silicon nanocrystals for color-neutral and transparent luminescent solar concentrators, ACS Photonics 6 (2019) 2303-2311.

[16] L. Etgar, D. Yanover, R.K. Čapek, R. Vaxenburg, Z. Xue, B. Liu, M.K. Nazeeruddin, E. Lifshitz, M. Grätzel, Core/shell PbSe/PbS QDs TiO$_2$ heterojunction solar cell, Adv. Funct. Mater. 23 (2013) 2736-2741.

[17] H. Zhao, D. Benetti, L. Jin, Y. Zhou, F. Rosei, A. Vomiero, Absorption enhancement in "giant" core/alloyed-shell quantum dots for luminescent solar concentrator, Small 12 (2016) 5354–5365.

[18] H. Li, K. Wu, J. Lim, H.-J. Song, V. I. Klimov, Doctor-blade deposition of

quantum dots onto standard window glass for low-loss large-area luminescent solar concentrators, Nat. Energy 1 (2016) 16157.

[19] V. I. Klimov, T. A. Baker, J. Lim, K. A. Velizhanin, H. McDaniel, Quality factor of luminescent solar concentrators and practical concentration limits attainable with semiconductor quantum dots, ACS Photonics 3 (2016) 1138-1148.

[20] H. Zhao, D. Benetti, X. Tong, H. Zhang, Y. Zhou, G. Liu, D. Ma, S. Sun, Z. M. Wang, Y. Wang, F. Rosei, Quality factor of luminescent solar concentrators and practical concentration limits attainable with semiconductor quantum dots, Nano Energy 50 (2018) 756-765.

[21] R. Connell, C. Pinnell, V. E. Ferry, Designing spectrally-selective mirrors for use in luminescent solar concentrators, J. Optics 20 (2018) 024009.

[22] D. R. Needell, O. Ilic, C. R. Bukowsky, Z. Nett, L. Xu, J. He, H. Bauser, B. G. Lee, J. F. Geisz, R. G. Nuzzo, A. P. Alivisatos, H. A. Atwater, Design criteria for micro-optical tandem luminescent solar concentrators, IEEE J. Photovolt. 8 (2018) 1560-1567.

[23] K. Wu, H. Li, V. I. Klimov, Tandem luminescent solar concentrators based on engineered quantum dots, Nature Photonics 12 (2018) 105-110.

[24] G. Liu, R. Mazzaro, Y. Wang, H. Zhao, A. Vomiero, High efficiency sandwich structure luminescent solar concentrators based on colloidal quantum dots, Nano Energy 60 (2019) 119-126.

[25] G. Iasilli, R. Francischello, P. Lova, S. Silvano, A. Surace, G. Pesce, M. Alloisio, M. Patrini, M. Shimizu, D. Comoretto, A. Pucci, Luminescent solar concentrators: boosted optical efficiency by polymer dielectric mirrors, Mater. Chem. Front. 3 (2019) 429-436.

[26] Y. Ghosh, B. D. Mangum, J. L. Casson, D. J. Williams, H. Htoon, J. A. Hollingsworth, New insights into the complexities of shell growth and the strong influence of particle volume in nonblinking "giant" core/shell nanocrystal quantum dots, J. Am. Chem. Soc. 134 (2012) 9634-9643.

[27] J. Wang, I. Mora-Sero, Z. Pan, K. Zhao, H. Zhang, Y. Feng, G. Yang, X. Zhong, J. Bisquert, Core/shell colloidal quantum dot exciplex states for the development of

highly efficient quantum-dot-sensitized solar cells, J. Am. Chem. Soc. 135 (2013) 15913-15922.

[28] F. Meinardi, A. Colombo, K. A. Velizhanin, R. Simonutti, M. Lorenzon, L. Beverina, R. Viswanatha, V. I. Klimov, S. Brovelli, Large-area luminescent solar concentrators based on 'Stokes-shift-engineered' nanocrystals in a mass-polymerized PMMA matrix, Nat. Photonics 8 (2014) 392-399.

[29] J. C. de Mello, H. F. Wittmann, R. H. Friend, An improved experimental determination of external photoluminescence quantum efficiency, Adv. Mater. 9 (1997) 230-232.

[30] M. Zhu, Y. Li, S. Tian, Y. Xie, X. Zhao, X. Gong, Deep-red emitting zinc and aluminium co-doped copper indium sulfide quantum dots for luminescent solar concentrators, J. Colloid Interf. Sci. 534 (2019) 509-517.

Click here to access/download
Supporting Information
SI.doc
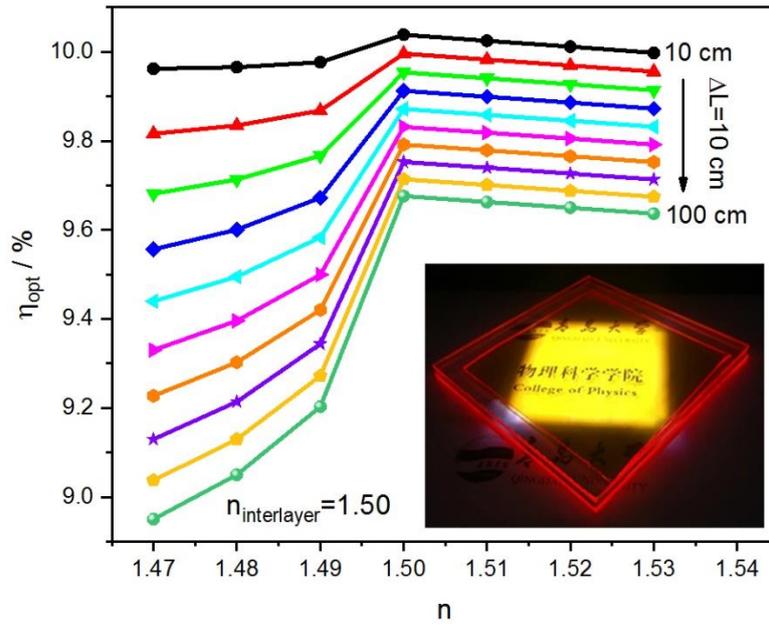
External optical efficiency of the laminated LSCs with different refractive index configuration. Inset is the photograph of the laminated LSCs based on CdSe/CdS QDs.